Published in final edited form as:

Nat Chem Biol. 2018 January ; 14(1): 15–21. doi:10.1038/nchembio.2513.

Ultrasensitive optical imaging with lanthanide lumiphores

Ukrae Cho[1], **Daniel P. Riordan**[2,4], **Paulina Ciepla**[1], **Kiranmai S. Kocherlakota**[1,5], **James K. Chen**[1,3,*], and **Pehr B. Harbury**[2,*]

[1]Department of Chemical and Systems Biology, Stanford University School of Medicine, Stanford, California 94305, USA

[2]Department of Biochemistry, Stanford University School of Medicine, Stanford, California 94305, USA

[3]Department of Developmental Biology, Stanford University School of Medicine, Stanford, California 94305, USA

Abstract

In principle, the millisecond emission lifetimes of lanthanide chelates should enable their ultrasensitive detection in biological systems by time-resolved optical microscopy. In practice, however, lanthanide imaging techniques have provided no better sensitivity than conventional fluorescence microscopy. Here, we identify three fundamental problems that have impeded lanthanide microscopy: low photon flux, inefficient excitation, and optics-derived background luminescence. We overcome these limitations with a new lanthanide imaging modality, trans-reflected illumination with luminescence resonance energy transfer (trLRET), which increases the time-integrated signal intensities of lanthanide lumiphores by 170-fold and the signal-to-background ratios by 75-fold. We demonstrate that trLRET provides at least an order-of-magnitude increase in detection sensitivity over conventional epifluorescence microscopy when used to visualize endogenous protein expression in zebrafish embryos. We also show that trLRET can be used to optically detect molecular interactions *in vivo*. trLRET promises to unlock the full potential of lanthanide lumiphores for ultrasensitive, autofluorescence-free biological imaging.

*Correspondence should be addressed to J.K.C. (jameschen@stanford.edu) or P.B.H. (harbury@stanford.edu).
[4]Present address: 10X Genomics, Pleasanton, California 94566, USA
[5]Present address: Chan-Zuckerberg Biohub and Department of Bioengineering, Stanford University School of Engineering, Stanford, California 94305, USA

AUTHOR CONTRIBUTIONS

K.S.K. and J.K.C. built the time-resolved LED epifluorescence microscope; P.B.H. conceived of LRET-enhanced imaging by tuning lanthanide lumiphore lifetimes; U.C. and P.B.H. conceived of, designed, and built the QSL trans-reflected illumination system; U.C., D.P.R., P. C., K.S.K., J.K.C, and P.B.H. designed the experiments; U.C. and P. C. performed the imaging experiments; U.C., D.P.R., P.C., K.S.K., J.K.C., and P.B.H. analyzed data; U.C., J.K.C., and P.B.H. wrote the paper.

COMPETING FINANCIAL INTERESTS

The authors declare no competing financial interests.

INTRODUCTION

Our ability to image molecular features within complex biological samples has improved dramatically over the last two decades. Synthetic and genetically encoded fluorescent probes with enhanced extinction coefficients and quantum yields have been developed[1,2], far-red fluorescent proteins have extended the spectral range of molecular imaging[3,4], and hybrid tandem fluorophores have facilitated single-molecule detection[5–8]. Yet molecules expressed at nanomolar or lower concentrations are still difficult to detect optically in cells and whole organisms. Weak probe signals are often overwhelmed by the autofluorescence associated with flavins, hemes, and other metabolites with conjugated π systems. Biological specimens treated with aldehyde crosslinking agents can also exhibit fixation-induced fluorescence to varying extents.

One promising approach for overcoming the autofluorescence of biological samples is the use of probes with long-lived photoluminescence. Lanthanide lumiphores have emission lifetimes in the millisecond regime, whereas those of biological fluorophores are typically less than 10 nanoseconds. Consequently, lanthanide-emitted photons can be differentiated from biological autofluorescence using pulsed excitation and time-delayed signal acquisition (Supplementary Fig. 1)[9,10]. Since the development of time-resolved luminescence microscopes in the early 1990s[11–14], dozens of lanthanide chelates have been synthesized for molecular imaging and metabolite sensing[15–19]. These complexes exhibit large Stokes shifts, narrow emission bands, photo-stability, and resistance to oxygen-mediated quenching. Solid-state pulsed light sources and intensified charge-coupled device (ICCD) cameras with single-photon sensitivity and sub-microsecond gating have also improved the capabilities of time-resolved microscopy.

Despite these advances, lanthanide probes are still not widely used for biological imaging. Lanthanide imaging systems have not yet achieved the signal intensities and detection sensitivities required for routine applications, and they do not surpass the capabilities of conventional fluorescence microscopy. This is paradoxical, given the predominance of lanthanide probes in ultrasensitive solution- and cell-based photometric assays[20–22]. Here we identify and solve three problems that have limited current lanthanide imaging systems. First, the millisecond excited-state lifetimes of lanthanides reduce their photon flux and imaging rates, limiting their utility for biological microscopy. Second, light-emitting diodes (LEDs) typically used for lanthanide imaging[10,23] excite only a small fraction of lanthanide probe within each imaging cycle, and this excitation efficiency decreases further as lanthanide emission rates increase. Third, the potential gains in signal-to-noise achieved by suppression of autofluorescence background are bounded by long-lived luminescence within the microscope objective lenses. This optics-derived luminescence is spectrally and temporally difficult to differentiate from lanthanide probe luminescence[24], and it degrades the signal-to-background ratios of the resulting images. In quantitative terms, a cutting-edge time-resolved microscope (equipped with a UV LED excitation source, an ICCD camera and optimized emission filters[24]) achieves signal-to-background ratios of ~7 when cells containing 1–10 μM lanthanide probe are imaged[25]. Thus, current lanthanide imaging technologies cannot surpass conventional fluorescence microscopy.

To address each of the challenges cited above, we have developed a new modality for time-resolved lanthanide imaging. Our approach, termed trans-reflected illumination with luminescence resonance energy transfer (trLRET), utilizes spectrally matched acceptor molecules to tune the emission rates and wavelengths of lanthanide lumiphores. In parallel, we use Q-switched laser (QSL) illumination to dramatically increase lanthanide excitation rates and consequently the excited-state fraction for each imaging cycle. In combination, these imaging modalities boost lanthanide-dependent signal intensities by 170-fold while still suppressing biological autofluorescence through temporal filtering. We also employ trans-illumination and ultraviolet (UV) light-reflecting coverslips to minimize optics-derived photoluminescence, improving probe detection sensitivities by 75-fold. Using lanthanide chelate-functionalized antibodies and diffusion-mediated LRET, we can now image endogenous proteins in zebrafish embryos with detection sensitivities and signal-to-background ratios that exceed what is possible with conventional fluorophores. We can also exploit proximity-dependent changes in LRET efficiency to visualize molecular interactions *in vivo*. Thus, trLRET opens the door to a new realm of ultrasensitive optical microscopy.

RESULTS

Identification of a lanthanide complex for in vivo imaging

To increase their brightness, lanthanide cations are typically complexed with a multi-dentate ligand bearing an energetically matched chromophore (commonly referred to as an 'antenna')[26]. Energy transferred from the excited antenna to the metal ion can then be dissipated through photon emission or non-radiative decay. Among the 15 lanthanides, Eu^{3+}, Gd^{3+}, and Tb^{3+} have electronic states that favor radiative pathways, with maximum emissions centered at red, ultraviolet, and green wavelengths, respectively[27]. Eu^{3+} complexes are best suited for biological applications since they can be excited by longer, less cytotoxic wavelengths of light (> 350 nm), and numerous organic ligands have been synthesized, including members of the EDTA, DTPA, TTHA, DOTA, triazacyclononane, terpyridine, and cryptand families[19,28,29]. Structurally diverse antennae have also been developed, such as coumarins, azaxanthones, acridones, 1-hydroxypyridin-2-ones, and tetraazatriphenylene.

Many of these luminescent Eu^{3+} complexes have sub-femtomolar dissociation constants in aqueous solutions[30]; however, the chelates can be sensitive to metabolites commonly found in cells. For example, trivalent lanthanide ions are efficiently sequestered by nucleoside triphosphates (NTPs and dNTPs) and inorganic phosphates[31]. Lanthanide luminescence can also be quenched by electron-rich metabolites such as ascorbate and urate[16]. We therefore sought to identify Eu^{3+} complexes that are appropriate for *in vivo* applications, focusing on the readily synthesized DTPA-cs124-CF_3 ligand[32] and commercially available ATBTA[33]. We observed that Eu^{3+}/ATBTA is considerably less sensitive to dNTPs and ascorbate-mediated quenching than Eu^{3+}/DTPA-cs124-CF_3 (Supplementary Fig. 2), perhaps due to the ability of the ATBTA ligand to engage all nine metal ion coordination sites and sterically block collisional quenching. We evaluated the Eu^{3+}/ATBTA chelate *in vivo* by coupling it to a morpholino oligonucleotide (MO) via cyanuric chloride and injecting the resulting Eu^{3+}/DTBTA-functionalized reagent into zebrafish zygotes. The embryos were then imaged using

a time-resolved epifluorescence microscope equipped with a 365-nm LED source, an ICCD camera, and a programmable digital delay generator[24,34]. The Eu^{3+}/DTBTA-MO-injected zygotes developed normally and exhibited long-lived Eu^{3+} emission signals for more than 3 days (Supplementary Fig. 3), demonstrating the efficacy of Eu^{3+}/DTBTA-based probes for biological applications.

LRET-accelerated lanthanide emission

Although the millisecond-scale luminescence lifetimes of lanthanide complexes enable the temporal filtering of autofluorescence, they also cause the emission rates to be 100,000-fold lower than for typical organic fluorophores, which have fluorescence lifetimes in the single-digit nanosecond scale. This slow emission severely limits the brightness of lanthanide lumiphores, and numerous imaging cycles are typically required to obtain adequate signal intensities. This is generally acceptable for photometric assays, such as those using microplate formats. However, the multiple seconds required to collect a time-resolved micrograph (< 1 kHz and 10^3–10^5 integrated cycles per image) match or exceed the timescales of many biological processes.

Lanthanide probes with excited-state lifetimes in the 0.1- to 10-μs regime would still enable time-gated removal of background autofluorescence and greatly increase photon output per unit time. We hypothesized that this could be realized by pairing luminescent lanthanide complexes with spectrally matched acceptors (Fig. 1a–b and Supplementary Fig. 1). The resulting LRET would bypass the parity-forbidden *f-f* transition to the lanthanide ground state, creating an alternative radiative pathway with faster kinetics and therefore shorter excited-state lifetimes. Like fluorescence resonance energy transfer, LRET can be achieved through the structural juxtaposition of lanthanide donors and acceptor fluorophores. Alternatively, freely diffusible acceptors can come within one Förster radius of a lanthanide donor during its excited-state lifetime and undergo energy transfer[35].

Using photometric measurements of homogenous solutions, we examined how the Eu^{3+}/ATBTA excited-state lifetime is affected by three potential LRET acceptors: Atto 610, Sulfo-Cy5, and Sulfo-Cy3. Each of the fluorophores reduced the average Eu^{3+}/ATBTA excited-state lifetime in a concentration-dependent manner, in proportion to their spectral overlap with the 614-nm emission line of the Eu^{3+}/ATBTA complex (Fig. 1c–d and Supplementary Fig. 4). Atto 610, which has a 615-nm excitation maximum and a 633-nm emission maximum, was the most efficient acceptor. A 10-μM concentration of this acceptor increased the decay rate of excited Eu^{3+}/ATBTA by 60-fold (τ = 1020 μs[33] versus 17 μs), leading to LRET luminescence with a 633-nm emission maximum. In addition, the greater quantum yield of Atto 610 in comparison to the Eu^{3+}/ATBTA complex (70% versus 38%; see Online Methods) resulted in a 1.8-fold signal enhancement (Fig. 1a). Thus, lanthanide complexes can be tuned to shorter excited-state lifetimes by controlling the spectral properties and local concentrations of fluorescent acceptors.

LRET-enhanced time-resolved lanthanide microscopy

We next investigated whether LRET could be used to increase the signal intensities of lanthanide probes during time-resolved microscopy (as depicted in Fig. 1b). We immobilized

Eu^{3+}/ATBTA onto agarose beads and immersed the resin in an aqueous solution with or without Atto 610. Using pulsed LED illumination, we observed average excited-state lifetimes of 36.0 ± 0.5 μs and 951 ± 41 μs, respectively, for the two conditions (Fig. 2a–b). We then imaged direct lanthanide emissions from the Eu^{3+}/ATBTA-conjugated beads using 1,500 imaging cycles at 450 Hz, each including a 1-μs excitation, a 1-μs delay, and a 2-ms signal acquisition time. Emissions in the presence of 10 μM Atto 610 were similarly detected using 60,000 imaging cycles at 18,000 Hz, each including a 1-μs excitation, a 1-μs delay, and a 50-μs signal acquisition time. The two protocols had identical total acquisition and imaging times (3 s and 3.3 s respectively, Fig. 2c), and we utilized a 575-nm longpass emission filter to simultaneously capture Eu^{3+}/ATBTA and Atto 610 emissions. The application of 1-μs LED pulses in both protocols also ensured that comparable excited-state levels were attained for each imaging cycle (see next section).

Based on the intrinsic and LRET-tuned lifetimes for the excited Eu^{3+}/ATBTA-conjugated beads and our emission acquisition parameters, the addition of Atto 610 should have increased the integrated lanthanide probe signal by 29-fold. The higher quantum yield of the LRET acceptor should improve this further, resulting in a 52-fold enhancement in luminescence intensity. In line with this expectation, the LRET-enhanced images exhibited pixel intensities that were 50-fold greater than those obtained by time-resolved microscopy without LRET enhancement (Fig. 2c).

LED illumination limits lanthanide excitation rates

The photoluminescence of lanthanide probes is influenced not only by their emission kinetics but also by their excitation rates. Signal intensities are proportional to the fraction of lumiphores that are excited in each imaging cycle, which itself is a function of the excitation and emission rate constants (k_{ex} and k_{em}, respectively) and illumination time (Supplementary Fig. 5). In the case of LRET-enhanced lanthanide detection, k_{ex} is dependent on the light source and donor structure and k_{em} varies with acceptor structure and concentration. Under these conditions, the excited-state fraction initially increases with longer excitation pulses. As the pulse width approaches the average excited-state lifetime ($\tau_{em} = 1/k_{em}$), the number of excited lanthanide probes begins to plateau with the steady-state maximum corresponding to $k_{ex}/(k_{ex} + k_{em})$.

We sought to determine the lanthanide excitation rate that could be achieved with an LED source, the standard illumination method for time-resolved lanthanide microscopy. We imaged Eu^{3+}/ATBTA-conjugated agarose beads with LED pulses of varying duration, both in the absence or presence of 10 μM Atto 610 (Fig. 2d–e). For these studies, we reduced the level of Eu^{3+}/ATBTA labeling on the agarose beads so that we could survey a broad range of excitation pulse widths (10 μs to 2 ms). Direct Eu^{3+}/ATBTA luminescence increased steadily with pulse width and began to plateau as excitation pulses exceeded 500 μs in length. In contrast, photoluminescence from Atto 610-treated Eu^{3+}/ATBTA beads reached a steady-state maximum that was approximately 20-fold lower in intensity. By combining these observations with our empirically measured average excited-state lifetimes (see Fig. 2a–b), we determined the excitation rate constant k_{ex} to be 357 s^{-1}.

Based on these findings, 25% of the Eu^{3+}/ATBTA complexes were in their excited state during continuous LED illumination (Fig. 2f). This steady-state population decreased to 1.3% when 10 μM Atto 610 acceptor was added. By extrapolation, the excited-state fraction of Eu^{3+}/ATBTA would be 0.035% when a 1-μs LED pulse width is applied in the presence of 10 μM Atto 610, negating the signal intensity enhancement afforded by faster emission rates and shorter imaging cycles. Thus, standard LEDs have insufficient radiant flux to realize the full potential of LRET-enhanced lanthanide imaging, and pulsatile light sources with greater photon flux are necessary.

Optics photoluminescence overlaps with lanthanide signals

Our studies of Eu^{3+}/ATBTA-labeled beads revealed another limiting factor for lanthanide imaging. When low bead-loading levels were employed, we unexpectedly observed background signals that impeded lanthanide probe imaging. We hypothesized that this background photoluminescence originated from UV light-excitable materials in the glass or in the optical coating of our microscope objective lenses. To investigate this possibility, we injected zebrafish zygotes with Eu^{3+}/DTBTA-functionalized 10-kDa dextran (30 fmol/embryo), which distributes uniformly among animal cells during development and is excluded from the yolk. We imaged the embryos at the 18-somite stage (16 hours post fertilization; hpf) using two objectives with similar magnifications and numerical apertures (5×/0.15 and 6.3×/0.13) but different 365-nm light transmission efficiencies (60% and 93%, respectively) (Fig. 3a). Steady-state imaging of the Eu^{3+}/DTBTA-injected embryos primarily captured yolk autofluorescence, while time-resolved imaging was able to selectively detect lanthanide luminescence and background instrument photoluminescence. The 6.3× objective with high UV-light transmittance yielded images with 3- to 5-fold higher signal-to-background ratios than the UV-absorbing objective (Fig. 3b), implicating the lens materials in the observed background photoluminescence.

In contrast to autofluorescence, these optics-derived signals could not be selectively suppressed through time-gated emission acquisition or the addition of a narrow bandpass filter (615/25 nm) (Fig. 3b). Since epifluorescence microscopes use objective lenses for both sample illumination and detection, optics photoluminescence is intrinsic to this imaging modality. Time-resolved lanthanide microscopy is particularly sensitive to these long-lived background signals.

Time-resolved lanthanide imaging with QSL trans-reflected illumination

Our findings revealed how current lanthanide microscopy platforms are constrained by their reliance on LED illumination and epifluorescence configurations. We therefore developed a new modality for time-resolved lanthanide imaging that overcomes both limitations. First, we replaced the LED source with a 355-nm QSL. The QSL can deliver several microjoules of light energy to the sample within 15 nanoseconds, whereas a UV LED source typically delivers less than 1 μJ of light in a 1-μs pulse. We also devised a trans-reflected illumination configuration that prevents UV light from reaching the microscope objective, thereby averting UV-induced luminescence from the lenses (Fig. 4a). This was accomplished by placing the sample on a TiO_2-coated coverglass that attenuates UV light by 100,000-fold but

selectively transmits longer-wavelength light with at least 90% efficiency (Supplementary Fig. 6).

To assess the efficacy of this system, we first examined its ability to minimize optics photoluminescence. We imaged Eu^{3+}/ATBTA-conjugated agarose beads using four different objectives in the LED epi-illumination and QSL trans-reflected illumination configurations (Fig. 4b). We again used beads with minimal Eu^{3+}/ATBTA labeling, which increased the relative contribution of optics-derived background to the total luminescence. When the beads were imaged with LED epi-illumination and standard objectives, we observed signal-to-background ratios between 1.2 and 3.0. This ratio could be improved to 5.6 by using an objective with high UV-light transmittance. When we imaged the Eu^{3+}/ATBTA-conjugated beads using QSL trans-illumination and the UV light-reflecting coverglass, the signal-to-background ratios were up to 75-fold higher than those obtained with LED epi-illumination.

We then asked whether the new illumination method could enable efficient imaging of biological samples. For this purpose, we compared images acquired through steady-state fluorescence microscopy versus time-resolved photoluminescence microscopy (Fig. 4c). Fixed 16-hpf zebrafish embryos were stained using an anti-myosin heavy chain 1E (MYH1E) primary antibody and secondary antibodies labeled with commonly used fluorophores (Alexa Fluor 405, 488, and 594) or Eu^{3+}/DTBTA. Fluorescence microscopy captured not only Alexa Fluor signals from the labeled somites but also yolk autofluorescence. In contrast, time-resolved microscopy using QSL trans-reflected illumination effectively minimized yolk autofluorescence and optics-derived background signals. As a result, the Eu^{3+}/DTBTA photoluminescence from the immunostained muscle cells was much more intense than the yolk-derived signals (Fig. 4c). By quantifying somite and yolk pixel intensities for each imaging configuration, we found that QSL trans-reflected imaging improved the signal-to-background ratio more than 25-fold relative to conventional epifluorescence microscopy.

We also compared the lanthanide excitation rates that could be achieved with LED epi-illumination versus QSL trans-reflected illumination. We injected zebrafish zygotes with Eu^{3+}/DTBTA-functionalized 10-kDa dextran (Fig. 5a) and imaged the embryos at the 26-somite stage (22 hpf). The signal intensity from the injected dextran increased with LED pulse width in a manner consistent with the previously measured excitation and emission rates (Fig. 2d), allowing pixel intensities to be correlated with the fraction of excited lumiphores (Fig. 5b). A 1-ms LED illumination pulse excited approximately 20% of the lanthanide complexes, whereas a 10-μs pulse excited only 0.35%. By comparison, a 25.7-μJ QSL pulse excited 36% of the probe molecules in 15 nanoseconds. Using these signal intensities and the rate equations described in Supplementary Fig. 5, we determined that the QSL k_{ex} values increased linearly with laser power, with the highest energy pulse (25.7 μJ) achieving a k_{ex} value of 29.3×10^6 s^{-1}—an 81,900-fold increase over the LED excitation rate constant (Supplementary Fig. 7). These excitation rates far exceed the k_{em} values for both intrinsic and LRET-enhanced lanthanide luminescence, and consequently excitation is never rate-limiting. Importantly, QSL trans-reflected illumination did not perturb zebrafish development and should therefore be compatible with live imaging (Supplementary Fig. 8). Optimized QSL imaging conditions, with 1-μJ pulses at 15 kHz, produced a time-averaged

sample irradiance of 60 mW/cm^2 (see Online Methods and Supplementary Table 1). This is smaller than the 95 mW/cm^2 irradiance produced under optimized LED imaging conditions, which used 1-ms excitation pulses at 240 Hz.

Integration of QSL trans-reflected illumination with LRET (trLRET)

QSL trans-reflected illumination and LRET enhancement should synergistically improve signal-to-background and luminescence intensity in lanthanide imaging. We quantified this improvement by comparing trLRET with the conventional LED epi-illumination format (Supplementary Fig. 9). We used imaging protocols that were independently optimized for the two modalities, taking into account cycle rates, quantum yields, excited-state fractions, and decay rates (Supplementary Fig. 10). First, we imaged Eu^{3+}/ATBTA beads, using 30 μM Atto 610 for the QSL trLRET condition (which reduced the luminescence lifetime of immobilized Eu^{3+}/ATBTA to 14 μs; see Supplementary Fig. 10). Since emission levels associated with the two methods differed by more than two orders of magnitude, we adjusted the camera gain to keep pixel intensities within a linear dynamic range (Supplementary Fig. 11). After normalizing for the differing gain values, we determined that QSL trLRET signal intensities were 170-fold greater than those obtained with a pulsed LED and no LRET enhancement (Supplementary Fig. 9).

We then compared the performance of LED epifluorescence and QSL trLRET imaging in zebrafish. We immunostained 18-hpf embryos with the anti-MYH1E primary antibody and a mixture of labeled and unlabeled secondary antibodies. The labeled secondary antibodies were conjugated to either Alexa Fluor 594- or Eu^{3+}/DTBTA (average labeling stoichiometry of 1.5 and 1.2 probes/antibody respectively, Fig. 6a and Supplementary Fig. 12). The total secondary antibody concentration was fixed at 0.5 μg/mL to avoid any potential concentration-dependent changes in antibody affinity, and the labeled population was varied from 10% to 100%. Whole-mount immunostaining of zebrafish embryos and larvae typically utilizes fluorescently tagged secondary antibodies at approximately 1–2 μg/mL. At lower antibody concentrations, the fluorescent signals are obscured by yolk and fixation-induced autofluorescence. Accordingly, we observed that 0.5 μg/mL Alexa Fluor 594-conjugated secondary antibody was required to visualize anti-MYH1E antibody-labeled somites by steady-state epifluorescence microscopy. When the embryos were imaged in the presence of 10 μM Atto 610 with the QSL trLRET system, the same primary antibody could be readily detected at a 10-fold lower concentration of Eu^{3+}/DTBTA-conjugated secondary antibody (Fig. 6a).

Quantitative comparisons of the somite and yolk pixel intensities, which reflect specific immunostaining signals versus yolk autofluorescence and non-specific antibody binding, confirmed that the new lanthanide-imaging modality outperformed epifluorescence microscopy (Fig. 6a). Even at the lowest tested concentration of Eu^{3+}/DTBTA-labeled secondary antibody, the somites in the trLRET images were 100-fold brighter than the yolk. Steady-state fluorescence images acquired with the same concentration of Alexa Fluor 594-conjugated secondary antibody had minimally detectable specific signals, with a somite-to-yolk ratio of 0.60. Taken together, our results illustrate how QSL trLRET can dramatically enhance the time-resolved imaging of lanthanide-based probes in whole organisms.

QSL trLRET imaging of molecular interactions in vivo

Like fluorescence resonance energy transfer (FRET), distance-dependent changes in intramolecular LRET efficiency can be employed to detect molecular interactions or conformational states[20,22,36]. To explore this capability in the context of trLRET imaging, we tested whether we could visualize the binding of two macromolecules in a live animal. We injected zebrafish zygotes with a Eu^{3+}/DTBTA-labeled MO and either a complementary or non-complementary MO labeled with Atto Rho14, an LRET acceptor that is stable *in vivo* (Fig. 6b). We then imaged the embryos at 24 hpf, using the QSL trLRET system. These studies utilized a 575-nm longpass filter to detect all emitted photons, and a 655/40-nm filter to selectively detect LRET-induced Atto Rho14 fluorescence. Embryos injected with the complementary MOs exhibited 13-fold higher LRET signal intensities than those injected with the non-complementary oligonucleotides. Thus, trLRET microscopy can be used to visualize biochemically regulated interactions *in vivo*.

DISCUSSION

Time-resolved lanthanide imaging has lagged behind fluorescence microscopy, and its biological applications have been largely restricted to cultured cells and single-celled organisms[10,14,23,24,36]. Here we demonstrate how QSL trans-reflected illumination and LRET-enhanced lanthanide decay can be used to overcome three key factors that have limited lanthanide imaging: low photon efflux, slow excitation rates, and optics-derived photoluminescence. These advances establish a new modality for time-resolved lanthanide imaging that can be readily applied to multicellular organisms, allowing the technology to surpass the detection limits of fluorescence microscopy for the first time.

The slow emission rates of photoluminescent lanthanide chelates intrinsically constrain imaging methods that capture direct lanthanide emissions. The signal integration times required to compensate for reduced lanthanide photon flux are often impractical for biological applications and lead to higher levels of dark noise. Since biological and fixation-induced autofluorescence decays within tens of nanoseconds, probe lifetimes in the 0.1- to 10-μs regime arguably provide the best balance between total imaging time and background suppression. Luminescent complexes containing the transition metals Ir^{3+}, Re^{+}, Ru^{2+}, or Pt^{2+} have emission lifetimes that fall within this range; however, these reagents are highly oxygen-sensitive, limiting their versatility as biological probes[37–40]. In comparison, lanthanide complexes are largely insensitive to chemical environment. As demonstrated by our studies, diffusion-mediated LRET is a simple and effective means for shortening lanthanide excited-state lifetimes to microsecond durations, improving the performance of lanthanide probes for time-resolved imaging. Exploiting LRET to achieve 50-fold increases in lanthanide brightness is conceptually distinct from previous applications of LRET to sense changes in molecular structure[36,41,42].

The instrumentation commonly used for time-resolved lanthanide imaging also has intrinsic limitations. LEDs excite only a small fraction of lanthanide complexes with each illumination pulse, particularly when LRET enhancement is used to achieve microsecond-scale emission lifetimes. In addition, epi-illumination generates optics-derived photoluminescence that has lanthanide-like properties, bounding the signal-to-background

improvements that can be achieved by autofluorescence suppression. QSL trans-reflected illumination addresses both of these issues. Since QSL photon flux is several thousand times greater than that of pulsed LEDs, a single QSL pulse can excite a substantial fraction of lanthanide probe molecules, even when LRET enhancement is employed. The trans-illumination configuration allows placement of a UV-reflecting coverglass between the sample and microscope objective, preventing the excitation of photoluminescent materials in the lenses. In principle, optics-derived background signals could be averted by other approaches such as reflective objectives[43,44], darkfield microscopy[45], and light sheet microscopy[46]. The planar illumination of light-sheet microscopy also suppresses sample autofluorescence and minimizes phototoxicity, and this method holds particular promise for time-resolved lanthanide imaging.

Using QSL trans-reflected illumination and time-resolved microscopy to image beads with minimal Eu^{3+}/ATBTA labeling, we observed signal-to-background ratios that were 75-fold higher than those obtained by LED epi-illumination. In addition, integrated signal intensities were 170-fold higher when QSL trans-reflected illumination was combined with diffusion-mediated LRET. These new capabilities are directly applicable to biological imaging, as illustrated by our studies of zebrafish embryos. We anticipate that trLRET will help establish lanthanide microscopy as a valuable tool for biological research, particularly for the detection of low-abundance proteins and transcripts in cells, tissues, or whole organisms. LRET-enhanced lanthanide imaging also has the potential for multiplexing, as individual lanthanide donor/acceptor pairs can be distinguished both spectrally and temporally[47,48]. Finally, lanthanide-based sensors have been used to visualize molecular interactions in cells[36] and our trLRET imaging system extends these capabilities to live organisms. Developing lanthanide chelates and probes with new functionalities will be important next steps toward realizing these capabilities.

ONLINE METHODS

Time-resolved luminescence and steady-state microscopy

Time-resolved imaging was conducted with a Leica DMI6000B inverted microscope, a Stanford Photonics XR/MEGA-10Z ICCD camera, a Prizmatix 365-nm light-emitting diode (Mic-LED-365), a Spectra-Physics 355-nm Q-switched laser (QSL) (Explorer One 355-300), and a Quantum Composers 4-channel pulse generator (Model 9514). Communication between the QSL and 4-channel pulse generator was mediated by a breakout board (Winford Engineering, LLC; BRKSD26HDF-R), a wire lead-to-BNC male cable (Pomona Electronics; 4970), and a BNC female-to-BNC male cable (AV-Cables.net). The integrated system was controlled with Piper Software (ICCD camera; version 2.6.84) and L-Win software (QSL; version 1.5.11), using the image acquisition parameters shown in Supplementary Table 2. Steady-state fluorescence imaging was conducted using a Photometric CoolSNAP HQ CCD camera, a Leica EL6000 external light source, and MetaMorph software (version 7.8), with the exception of the data set for Supplementary Fig. 8. For those micrographs, a Leica DM4500B upright compound microscope equipped with a 5×/0.12 N Plan objective and a Retiga-SRV Fast 1394 camera was used. Images were acquired with the following objectives: HCX PL S-APO 5×/0.15 NA, HCX PL FLUOTAR

UVI 6.3×/0.13, HCX PL FLUOTAR 10×/0.30, and HCX PL FLUOTAR L 20×/0.40. Filter sets used in these studies were: DAPI (Ex: 360/40 nm; Em: 470/40 nm), GFP (Ex: 470/40 nm; Em: 525/50 nm), TX2 (Ex: 560/40 nm; Em: 645/75 nm), and lanthanide (Ex: 360/40 nm; Em: > 575 nm). Further details about the LED and QSL illumination methods are provided in Supplementary Table 1. The QSL trans-illumination set-up is depicted in Supplementary Fig. 13. Briefly, a cage system was built around the microscope body using UV-enhanced aluminum mirrors (Thorlabs; PF10-03-F01) to direct the QSL beam to the stage. This trans-illumination light path projected a 4-mm illuminated disc with an area of 0.126 cm^2 onto the sample. Light pulses of 1 μJ at 15,000 Hz were typically used for QSL trLRET imaging. After accounting for the 50% transmission efficiency from laser to stage, this corresponds to 7500 μJ/s or equivalently 7.5 mW of power. The time-averaged irradiance at the sample was therefore 7.5/0.126 = 60 mW/cm^2.

TiO_2-coated coverslips for trLRET imaging

The following coverslips were coated with TiO_2 at IOS Optics (Santa Clara, CA): 0.25- and 0.50-mm thick, 25.4-mm diameter sapphire (Ted Pella 16005-1010 and 16005-1020); 0.2-mm thick, 25.4-mm diameter fused quartz (Technical Glass Products); No. 1.5, 25.4-mm diameter borosilicate glass (Warner Instruments 64-0715). No thermal damage or mechanical warping was observed during the coating process. An overlying protective SiO_2 layer was also added. Upon QSL illumination, the sapphire and fused quartz coverslips did not generate any detectable background, while some long-lived photoluminescence was observed from the coated borosilicate coverslips. All experiments were performed with the sapphire coverslips due to ease of handling and the absence of background emission.

Zebrafish embryo injections and imaging

All zebrafish experiments were conducted with wild-type AB fish (Zebrafish International Resource Center), in compliance with protocol 10511 approved by the Stanford University Institutional Animal Care and Use Committee. Embryos were obtained by natural mating and cultured in E3 medium at 28 °C. All embryo injections (typically 1–2 nL/embryo) were conducted in E3 medium at room temperature. For live-imaging studies, the embryos were manually dechorionated and then immobilized in E3 medium containing 1.5% (w/v) low melting point agarose. Animal studies were conducted without blinding.

Preparation of Eu^{3+}/ATBTA-functionalized beads

Eu^{3+}/ATBTA (TCI) was dissolved in 20 mM HEPES buffer (pH 8) to prepare a 1 mM solution of the lanthanide complex. N-hydroxysuccinimide (NHS) ester-activated agarose beads (1 mg; Thermo Scientific) were shaken in 0.5 mL of the 1 mM Eu^{3+}/ATBTA solution at room temperature for either 1 minute or 16 hours, depending on the desired degree of Eu^{3+}/ATBTA loading. Low loading levels were utilized to determine lanthanide excitation rates and to establish methods for minimizing optics-derived photoluminescence and maximizing lanthanide detection sensitivity. The reaction was then centrifuged to remove supernatant, and the beads were washed with 20 mM HEPES buffer (pH 8) (3 × 0.5 mL) prior to use.

Homogeneous solution assays

Lanthanide luminescence in homogeneous solutions was measured with a Tecan Infinite M1000 Pro microtiter plate reader, using the instrument configurations described in Supplementary Table 3. Sulfo-Cy3 and Sulfo-Cy5 reagents were purchased from Lumiprobe; Atto 610 and sodium ascorbate from Sigma-Aldrich; and dNTPs from Life Technologies. To determine the lifetimes of LRET-mediated lanthanide luminescence, signal intensities were measured for a series of 'time slices.' Collection times were fixed at 100 μs, and the temporal delay was varied from 0 to 400 μs. The integrated signal intensities of these time slices were fitted to the equation below using MATLAB software (version R2015b).

$$y(t)=c\times\int_{\text{delay}}^{\text{delay}+100}e^{-t/\tau}\,\mathrm{dt}$$

To compare the integrated signal intensities of Eu^{3+}/ATBTA complexes in the absence and presence of 10 μM Atto 610 (i.e., integrated emission spectra from 0 μs after excitation to infinity), emission photons were collected for 2 ms (maximum collection time permitted by the instrument) after a delay of 30 μs. The measured signal intensities for this pulse cycle and average luminescence lifetimes (1020 and 17 μs in the absence and presence of Atto 610, respectively) were then used to calculate total photon emissions for each experimental condition.

Determination of the Eu^{3+}/ATBTA quantum yield (QY_{Eu})

LRET emission is $(E_{LRET}\times QY_{acceptor})/QY_{Eu}$ times brighter than direct Eu^{3+} emission (Fig. 1a). In the presence of 10 μM Atto 610, we observed that LRET emission is 1.8-fold more efficient than the direct Eu^{3+} emission for the Eu^{3+}/ATBTA complex, as determined by comparing their integrated spectra (Fig. 1d). Since E_{LRET} under these conditions is 98% ($1-\tau_{+LRET}/\tau_{-LRET}$) and the quantum yield of Atto 610 is reported to be 70%, we estimate the Eu^{3+}/ATBTA quantum yield to be 38%.

Diffusion-enhanced LRET curve fitting

LRET-enhanced lanthanide luminescence was modeled using equations 1 and 2, as previously described[35].

$$E_{LRET}=\frac{k_r}{k_0+k_r}=1-\frac{\tau}{\tau_0}\quad(1)$$

E_{LRET}: LRET efficiency

τ: lanthanide complex lifetime in the presence of an acceptor

τ_0: lanthanide complex lifetime in the absence of an acceptor

k_0: rate constant for lanthanide emission in the absence of an acceptor = $1/\tau_0$

k_r: rate constant for the energy transfer

$$k_r = \frac{4\pi\rho {R_0}^6}{3\tau_0 a^3} \quad (2)$$

ρ: density of acceptor molecules (concentration)

R_0: distance between the donor and acceptor at which the LRET efficiency is 50%

a: distance of closest approach between the donor and acceptor

Equation 2 can be simplified as $k_r = c \times \rho / \tau_0$, where c is a constant for a given LRET pair. Using this abridged description of k_r and defining $k_0 = 1/\tau_0$, equation 1 can be re-written as equation 3. This can be further simplified to equation 4, which shows the relationship between the acceptor concentration (ρ) and LRET lifetime (τ).

$$\frac{\frac{c\rho}{\tau_o}}{\frac{1}{\tau_0}+\frac{c\rho}{\tau_0}} = 1 - \frac{\tau}{\tau_o} \quad (3)$$

$$\tau = \tau_0 \left(\frac{1}{1+c\rho}\right) \quad (4)$$

Synthesis of cs124-CF_3 (7-amino-4-trifluoromethyl-2(1H)-quinolinone)

cs124-CF_3 was prepared according to a previously reported procedure[48]. 1,3-phenylenediamine (100 mg, 0.925 mmol), zinc chloride (139 mg, 1.02 mmol), and ethyl 4,4,4-trifluoroacetoacetate (187 mg, 0.925 mmol) were dissolved in 1 mL DMSO. The reaction mixture was stirred at 150 °C for 48 hours. After cooling to room temperature, the reaction was added to 10 mL water, and extracted with diethyl ether (3 × 20 mL). The organic layers were combined, dried over anhydrous $MgSO_4$, and concentrated under reduced pressure. The crude product was purified by silica gel chromatography eluting with hexane/EtOAc (from 4:1 to 1:4), affording a beige powder (47.6 mg, 22.6 %). ^{1}H NMR (400 MHz, CD_3OD) δ= 6.53 (s, 1H), 6.55 (s, 1H), 6.68 (d, J = 7.2 Hz, 1H), 7.50 (d, J = 7.2 Hz, 1H). HRMS-ESI (m/z): $[M + H]^+$ calculated for $C_{10}H_8O_1N_2F_3$, 229.0583; observed, 229.0590.

Synthesis of DTPA-cs124-CF_3 (diethylenetriaminepentaacetic acid-7-amino-4-trifluoro-methyl-2(1H)-quinolinone)

DTPA-cs124-CF_3 was prepared according to a previously reported procedure[20]. DTPA (diethylenetriaminepentaacetic acid) dianhydride (17.2 mg, 0.0481 mmol) and triethylamine (58.0 mg, 0.573 mmol) were dissolved in 1.1 mL DMF. To this solution, cs124-CF_3 (9.0 mg, 0.039 mmol) in 0.5 mL DMF was added dropwise. After stirring at room temperature for 1 hour, the reaction was quenched with 3.5 mL of 1M triethylammonium acetate (pH 6.5). The reaction product was then purified by HPLC. Yield: 10.0 mg (42.5 %). ^{1}H NMR (400 MHz, CD_3OD) δ = 3.25 (m, 4H), 3.55 (m, 4H), 3.65 (m, 6H), 3.75 (s, 2H), 4.45 (s, 2H), 6.88 (s,

1H), 7.40 (d, J = 8.5 Hz, 1H), 7.76 (d, J = 8.5 Hz, 1H), 8.18 (s, 1H). HRMS-ESI (m/z): $[M + H]^+$ calculated for $C_{24}H_{29}O_{10}N_5F_3$, 604.1861; observed, 604.1849.

Synthesis of Eu^{3+}/DTBTA (cyanuric chloride-activated Eu^{3+}/ATBTA)

Eu^{3+}/ATBTA (1.2 mg, 1.4 μmol) was dissolved in ice-cold 0.1 M acetate buffer (pH 5; 60 μL). To this solution was added cyanuric chloride (0.70 mg, 3.8 μmol; Aldrich) in ice-cold acetone (25 μL). After the reaction mixture was incubated at 10 °C for 120 minutes, acetone (1 mL) was added dropwise. The resulting precipitate was pelleted by centrifugation at 17,000 *g* for 1 minute, washed with acetone (2 × 0.5 mL), and dried *in vacuo* to obtain Eu^{3+}/DTBTA as a yellow powder (80–90% yield). The full conversion of Eu^{3+}/ATBTA to Eu^{3+}/DTBTA was confirmed by LC/MS analysis. HRMS-ESI (m/z): $[M - H]^-$ calculated for $C_{40}H_{30}O_8N_9Cl_2Eu$, 986.0734; observed, 986.0714. The Eu^{3+}/DTBTA was then stored as a 1.5 mM aqueous solution at −20 °C.

Preparation of labeled secondary antibodies

Goat anti-mouse IgG (100 μL, Jackson ImmunoResearch, product number 115-005-146 (Fig. 4c) or Thermo Fisher Scientific, product number 31160 (Fig. 6a and Supplementary Fig. 12)) was dialyzed against conjugation buffer (150 mM NaCl and 10 mM HEPES, pH 8) at room temperature and 4 °C (3 × 300 mL; 2 hours, 2 hours, and overnight), using a 10-kDa molecular weight cut-off dialysis cup (Thermo Scientific). A ~ 1 mM solution of Eu^{3+}/DTBTA or Alexa Fluor 594 NHS ester (Thermo Fisher Scientific, product number A20004) in ice-cold conjugation buffer was prepared immediately before use, and 5 μL of this solution was added to 100 μL of the dialyzed antibody solution. After the reaction mixture was incubated at room temperature overnight, unreacted Eu^{3+}/DTBTA was removed by two rounds of size-exclusion chromatography (Illustra MicroSpin G-50; GE Healthcare Life Sciences). The resulting stock solution of Eu^{3+}/DTBTA-labeled and Alexa Fluor 594-labeled secondary antibody appeared red-fluorescent upon 365-nm illumination. The probe-to-antibody ratios were calculated from absorbance levels at 341 nm (Eu^{3+}/DTBTA), 594 nm (Alexa Fluor 594), and 280 nm (antibody) as determined with a NanoDrop spectrophotometer (Thermo Scientific).

Preparation of labeled MOs

Eu^{3+}/DTBTA-labeled MO: A non-targeting control morpholino (5'–GACAACCACTACCTGAGCACCCAGT–3'; Gene Tools, LLC) with a 3' primary amine (6 nmol) was incubated with Eu^{3+}/DTBTA (56 nmol) in 0.2 M HEPES (100 μL, pH 8) buffer, and the reaction mixture was shaken at room temperature overnight in the dark. Excess Eu^{3+}/DTBTA was removed by size-exclusion chromatography (NAP-5 column (GE Healthcare Life Sciences) and/or a Sep-Pak C18 1 cc Vac cartridge (Waters)) to obtain the Eu^{3+}/DTBTA-labeled morpholino. MS-ESI: m/z calculated for $C_{336}H_{496}O_{105}N_{158}P_{25}Cl_1Eu_1$ $[M + H]^+$: 9390; observed: 9390. Atto Rho14-labeled MOs: A morpholino (5'–ACTGGGTGCTCAGGTAGTGG TTGTC–3' or 5'–GCTGTTGTAGTTGTACTCCAGCTTG–3') with a 5' primary amine (6 nmol) was incubated with Atto Rho14 NHS ester (41 nmol; Sigma) in 0.2 M HEPES buffer (70 μL; pH 8) and DMSO (10 μL), and the reaction mixture was shaken at room temperature for 4 hours in the dark. Excess Atto Rho14 NHS ester was removed by size-exclusion chromatography.

MS-ESI (m/z): (1) $[M + H]^+$ calculated for $C_{312}H_{487}O_{109}N_{151}P_{25}$ + 766.6 (Atto Rho14), 9638; observed, 9638 and (2) $[M + H]^+$ calculated for $C_{311}H_{489}O_{111}N_{143}P_{25}$ + 766.6 (Atto Rho14), 9548; observed, 9548.

Preparation of Eu^{3+}/DTBTA-labeled dextran

10-kDa dextran amine (1 nmol; Molecular Probes) in 7.5 μL conjugation buffer (150 mM NaCl and 10 mM HEPES, pH 8) was added to a 1.2 mM solution of Eu^{3+}/DTBTA (7.5 μL) in the same buffer. The reaction mixture was incubated at room temperature for 3 h in the dark. Excess Eu^{3+}/DTBTA was then removed by size-exclusion chromatography (Illustra MicroSpin G-50; GE Healthcare Life Sciences).

Immunostaining of zebrafish embryos

(See Supplementary Table 4 for the primary and secondary antibodies used for respective experiments). Wild-type AB zebrafish embryos at the desired developmental stage were dechorionated in E3 medium and fixed in freshly prepared 4% paraformaldehyde in PBS for 90 minutes at room temperature. After fixation, the embryos were washed with PBS containing 0.5% (v/v) Triton X-100 (4 × 1 mL; 10 minutes per wash) and treated for 90 minutes at room temperature with a 1-mL aqueous solution of 10 mM Tris-HCl (pH 7.5), 250 mM NaCl, 10% (v/v) sheep serum, 0.5% (v/v) Triton X-100, and 0.5% (w/v) bovine serum albumin. After the blocking solution was removed, the embryos were incubated with anti-MYH1E antibody (1:15 dilution, Developmental Studies Hybridoma Bank, MF20) at 4 °C overnight in 500 μL blocking solution. The primary antibody solution was then removed, and the embryos were washed with a 1-mL solution of 10 mM Tris-HCl (pH 7.5), 250 mM NaCl, and 0.5% (v/v) Triton X-100 (TBSX) (4 × 5 minutes and then 3 × 20 minutes). After 90 minutes of additional blocking, the embryos were incubated with varying dilutions of pre-adsorbed Alexa Fluor- or Eu^{3+}/DTBTA-labeled secondary antibody in 500 μL blocking solution for 1.5 hours at room temperature. (The secondary antibodies were pre-adsorbed against 20–30 fixed zebrafish embryos as a 1:500 dilution in 1 mL blocking solution for 1.5 hours at room temperature) The samples were subsequently washed with 1 mL TBSX (5 × 5 minutes and then 3 × 20 minutes) and mounted in an aqueous solution containing 1.5% (w/v) low melting point agarose. For trLRET imaging, embryos were incubated in TBSX supplemented with 30 μM Atto 610 for 15 minutes, and then mounted in a low melting point agarose containing the same concentration of Atto 610.

Image and statistical analyses

Quantitative analyses of bead micrographs utilized at least three beads per imaging condition, with each bead corresponding to several thousand pixels. For zebrafish imaging experiments, embryos were obtained from at least two breeding tanks, each containing 2–4 males and 2–4 females from separate adult stocks. The embryos were collected within the first 15 minutes of natural mating, pooled, and then randomly distributed. No blinding was applied. Quantitative analyses of zebrafish micrographs utilized at least three embryos per imaging condition, with each embryo corresponding to several hundred thousand pixels. Background levels were based on adjacent regions composed of several thousand pixels. To determine somite-to-yolk ratios, image analyses utilized circumscribed regions within

somitic (several thousand pixels) or yolk (tens of thousands of pixels) tissues. The *P*-value in Supplementary Fig. 9c was calculated using a two-tailed t-test assuming equal variance.

Supplementary Material

Refer to Web version on PubMed Central for supplementary material.

Acknowledgments

This paper is dedicated to the memory of M. Buchin, whose technical expertise was invaluable for this project. We also thank D. Callard and J. Stepkowski (Stanford Photonics) for their assistance with our ICCD camera, C. Limouse for discussions about optical design and alignment, and D. Fitzpatrick and G. Gatmaitan (IOS Optics) for the design and fabrication of TiO_2-coated coverglasses. This work was supported by a Samsung Scholarship (U.C.), a Stanford School of Medicine Dean's Fellowship (P.C.) the National Institutes of Health (DP1 HD075622 to J.K.C. and U01 HL099997 to P.B.H.) the National Science Foundation (CHE-1344038 to J.K.C.), and a Stanford ChEM-H Institute Seed Grant (J.K.C. and P.B.H.).

References

1. Grimm JB, Heckman LM, Lavis LD. The chemistry of small-molecule fluorogenic probes. Prog. Mol. Biol. Transl. Sci. 2013; 113:1–34. [PubMed: 23244787]
2. Rodriguez EA, et al. The growing and glowing toolbox of fluorescent and photoactive proteins. Trends Biochem. Sci. 2016; 42:111–129. [PubMed: 27814948]
3. Shu X, et al. Mammalian expression of infrared fluorescent proteins engineered from a bacterial phytochrome. Science. 2009; 324:804–807. [PubMed: 19423828]
4. Shcherbakova DM, Verkhusha VV. Near-infrared fluorescent proteins for multicolor in vivo imaging. Nat. Methods. 2013; 10:751–754. [PubMed: 23770755]
5. Bertrand E, et al. Localization of ash1 mrna particles in living yeast. Mol. Cell. 1998; 2:437–445. [PubMed: 9809065]
6. Raj A, van den Bogaard P, Rifkin SA, van Oudenaarden A, Tyagi S. Imaging individual mrna molecules using multiple singly labeled probes. Nat. Methods. 2008; 5:877–879. [PubMed: 18806792]
7. Choi HMT, et al. Programmable in situ amplification for multiplexed imaging of mrna expression. Nat. Biotechnol. 2010; 28:1208–1212. [PubMed: 21037591]
8. Tanenbaum ME, Gilbert LA, Qi LS, Weissman JS, Vale RD. A protein-tagging system for signal amplification in gene expression and fluorescence imaging. Cell. 2014; 159:635–646. [PubMed: 25307933]
9. Connally RE, Piper JA. Time-gated luminescence microscopy. Ann. N. Y. Acad. Sci. 2008; 1130:106–116. [PubMed: 18596339]
10. Jin D, et al. How to build a time-gated luminescence microscope. Curr. Protoc. Cytom. 2014; 67(Unit 2):22. [PubMed: 24510771]
11. Beverloo H, van Schadewijk A, van Gelderen-Boele S, Tanke H. Inorganic phosphors as new luminescent labels for immunocytochemistry and time-resolved microscopy. Cytometry. 1990; 11:784–792. [PubMed: 2272243]
12. Marriott G, Clegg RM, Arndt-Jovin DJ, Jovin TM. Time resolved imaging microscopy. Phosphorescence and delayed fluorescence imaging. Biophys. J. 1991; 60:1374–1387. [PubMed: 1723311]
13. Seveus L, et al. Time-resolved fluorescence imaging of europium chelate label in immunohistochemistry and in situ hybridization. Cytometry. 1992; 13:329–338. [PubMed: 1326429]
14. Marriott G, Heidecker M, Diamandis EP, Yan-Marriott Y. Time-resolved delayed luminescence image microscopy using an europium ion chelate complex. Biophys. J. 1994; 67:957–965. [PubMed: 7811952]

15. Moore EG, Jocher CJ, Xu J, Werner EJ, Raymond KN. An octadentate luminescent eu(iii) 1,2-hopo chelate with potent aqueous stability. Inorg. Chem. 2007; 46:5468–5470. [PubMed: 17567001]
16. Montgomery CP, Murray BS, New EJ, Pal R, Parker D. Cell-penetrating metal complex optical probes: Targeted and responsive systems based on lanthanide luminescence. Acc. Chem. Res. 2009; 42:925–937. [PubMed: 19191558]
17. Bünzli J-CG, Bünzli J-CG. Lanthanide luminescence for biomedical analyses and imaging. Chem. Rev. 2010; 110:2729–2755. [PubMed: 20151630]
18. Xu J, et al. Octadentate cages of tb(iii) 2-hydroxyisophthalamides: A new standard for luminescent lanthanide labels. J. Am. Chem. Soc. 2011; 133:19900–19910. [PubMed: 22010878]
19. Heffern MC, Matosziuk LM, Meade TJ. Lanthanide probes for bioresponsive imaging. Chem. Rev. 2013; 114:4496–4539. [PubMed: 24328202]
20. Dickson EF, Pollak A, Diamandis EP. Ultrasensitive bioanalytical assays using time-resolved fluorescence detection. Pharmacol. Ther. 1995; 66:207–235. [PubMed: 7667396]
21. Hagan AK, Zuchner T. Lanthanide-based time-resolved luminescence immunoassays. Anal. Bioanal. Chem. 2011; 400:2847–2864. [PubMed: 21556751]
22. Emami-Nemini A, et al. Time-resolved fluorescence ligand binding for g protein–coupled receptors. Nat. Protoc. 2013; 8:1307–1320. [PubMed: 23764938]
23. Connally R, Jin D, Piper J. High intensity solid-state uv source for time-gated luminescence microscopy. Cytometry A. 2006; 69:1020–1027. [PubMed: 16888769]
24. Gahlaut N, Miller LW. Time-resolved microscopy for imaging lanthanide luminescence in living cells. Cytometry A. 2010; 77A:1113–1125.
25. Rajendran M, Miller LW. Evaluating the performance of time-gated live-cell microscopy with lanthanide probes. Biophys. J. 2015; 109:240–248. [PubMed: 26200860]
26. Moore EG, Samuel AP, Raymond KN. From antenna to assay: Lessons learned in lanthanide luminescence. Acc. Chem. Res. 2009; 42:542–552. [PubMed: 19323456]
27. Bunzli JC, Piguet C. Taking advantage of luminescent lanthanide ions. Chem. Soc. Rev. 2005; 34:1048–1077. [PubMed: 16284671]
28. Armelao L, et al. Design of luminescent lanthanide complexes: From molecules to highly efficient photo-emitting materials. Coord. Chem. Rev. 2010; 254:487–505.
29. Mathis, G., Bazin, H. Lanthanide luminescence. Springer; 2011. p. 47-88.
30. Byegård J, Skarnemark G, Skålberg M. The stability of some metal edta, dtpa and dota complexes: Application as tracers in groundwater studies. J. Radioanal. Nucl. Chem. 1999; 241:281–290.
31. Firsching FH, Brune SN. Solubility products of the trivalent rare-earth phosphates. J. Chem. Eng. Data. 1991; 36:93–95.
32. Chen J, Selvin PR. Synthesis of 7-amino-4-trifluoromethyl-2-(1h)-quinolinone and its use as an antenna molecule for luminescent europium polyaminocarboxylates chelates. J. Photochem. Photobiol. A. 2000; 135:27–32.
33. Nishioka T, et al. New luminescent europium(iii) chelates for DNA labeling. Inorg. Chem. 2006; 45:4088–4096. [PubMed: 16676970]
34. Hanaoka K, Kikuchi K, Kobayashi S, Nagano T. Time-resolved long-lived luminescence imaging method employing luminescent lanthanide probes with a new microscopy system. J. Am. Chem. Soc. 2007; 129:13502–13509. [PubMed: 17927176]
35. Thomas DD, Carlsen WF, Stryer L. Fluorescence energy transfer in the rapid-diffusion limit. Proc. Natl. Acad. Sci. U. S. A. 1978; 75:5746–5750. [PubMed: 16592590]
36. Rajapakse HE, et al. Time-resolved luminescence resonance energy transfer imaging of protein-protein interactions in living cells. Proc. Natl. Acad. Sci. U. S. A. 2010; 107:13582–13587. [PubMed: 20643966]
37. Yam VW, Wong KM. Luminescent metal complexes of d6, d8 and d10 transition metal centres. Chem. Commun. 2011; 47:11579–11592.
38. Thorp-Greenwood FL, Balasingham RG, Coogan MP. Organometallic complexes of transition metals in luminescent cell imaging applications. J. Organomet. Chem. 2012; 714:12–21.

39. Botchway SW, et al. Time-resolved and two-photon emission imaging microscopy of live cells with inert platinum complexes. Proc. Natl. Acad. Sci. U. S. A. 2008; 105:16071–16076. [PubMed: 18852476]

40. de Haas RR, et al. Phosphorescent platinum/palladium coproporphyrins for time-resolved luminescence microscopy. J. Histochem. Cytochem. 1999; 47:183–196. [PubMed: 9889254]

41. Selvin PR. Lanthanide-based resonance energy transfer. IEEE. J. Sel. Topics Quantum Electron. 1996; 2:1077–1087.

42. Kubota T, et al. Mapping of voltage sensor positions in resting and inactivated mammalian sodium channels by lret. Proc. Natl. Acad. Sci. U. S. A. 2017; 114:E1857–E1865. [PubMed: 28202723]

43. Norris KP, Seeds WE, Wilkins MHF. Reflecting microscopes with spherical mirrors. J. Opt. Soc. Am. 1951; 41:111–119.

44. Miyata S, Yanagawa S, Noma M. Reflecting microscope objectives with nonspherical mirrors. J. Opt. Soc. Am. 1952; 42:431–432.

45. Witlin B. Darkfield illuminators in microscopy. Science. 1945; 102:41–42. [PubMed: 17787422]

46. Huisken J, Swoger J, Del Bene F, Wittbrodt J, Stelzer EH. Optical sectioning deep inside live embryos by selective plane illumination microscopy. Science. 2004; 305:1007–1009. [PubMed: 15310904]

47. Lu Y, et al. Tunable lifetime multiplexing using luminescent nanocrystals. Nature Photon. 2014; 8:32–36.

48. Chen JY, Selvin PR. Lifetime- and color-tailored fluorophores in the micro- to millisecond time regime. J. Am. Chem. Soc. 2000; 122:657–660.

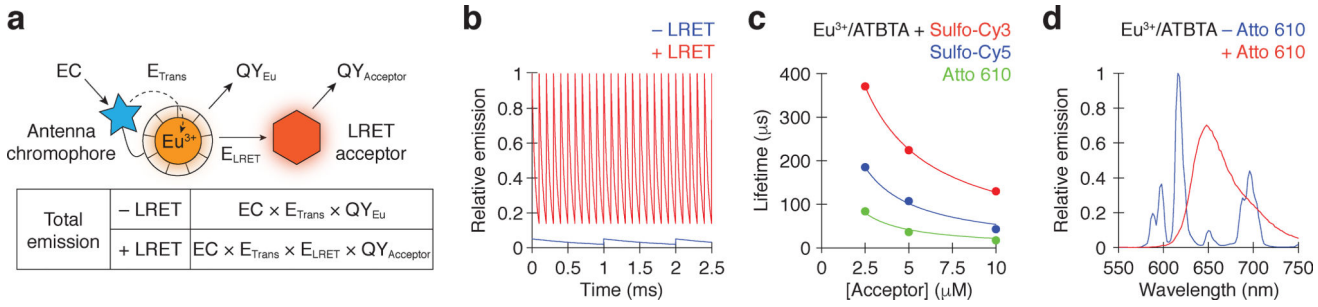

Figure 1. Time-resolved lanthanide detection and LRET enhancement

(a) Energy cascades involved in direct Eu^{3+} chelate and LRET emissions. E_{LRET} is given by $1 - \tau_{+LRET}/\tau_{-LRET}$. (b) Emission rate profiles associated with conventional (blue; τ = 1,000 μs and pulse interval = 1,000 μs) and LRET-enhanced (red;τ = 50 μs and pulse interval = 100 μs) time-resolved microscopy, assuming equivalent total emissions for each excited state. (c) Concentration-dependent reduction of Eu^{3+}/ATBTA emission lifetimes by spectrally distinct LRET acceptors (Sulfo-Cy3, Sulfo-Cy5, and Atto 610; 1 μM Eu^{3+}/ATBTA). The data were fit to a diffusion-enhanced LRET model (see Online Methods), yielding R^2 values of 1.00, 0.987, and 0.973, respectively. (d) Emission spectra of 1 μM Eu^{3+}/ATBTA in the presence and absence of 10 μM Atto 610.

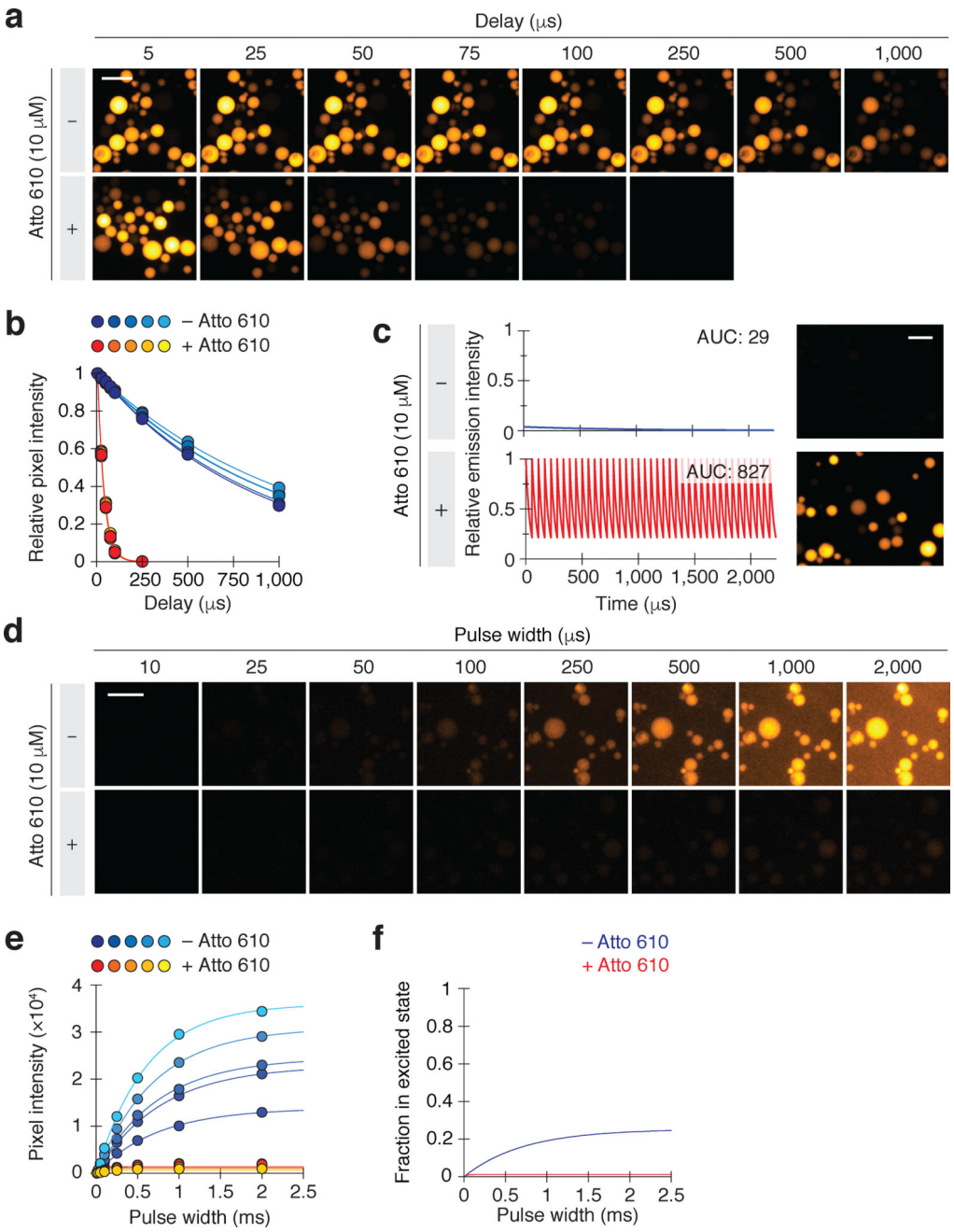

Figure 2. LRET-enhanced time-resolved imaging of lanthanide-functionalized beads

(a) Representative time-resolved images of Eu^{3+}/ATBTA-functionalized beads in the absence or presence of 10 μM Atto 610. Each imaging cycle included a 10-μs excitation pulse, the indicated delay, and a 500-μs emission acquisition period. (b) Average pixel intensities of representative individual beads in (a). The data were fit to a first-order decay model to obtain emission lifetimes for the immobilized Eu^{3+}/ATBTA in the absence or presence of 10 μM Atto 610: 951 ± 41 μs and 36.0 ± 0.5 μs, respectively (s.e.m., n = 5 beads). Scale bar: 200 μm. (c) Comparison of conventional and LRET-enhanced time-resolved imaging of Eu^{3+}/ATBTA-functionalized beads. Total imaging time was identical for

each condition, with individual cycles including a 1-μs excitation pulse, 1-μs delay, and either a 2,000-μs (− Atto 610) or 50-μs (+ Atto 610) acquisition period. Emission curves were plotted assuming identical quantum yields for direct and LRET-mediated photoluminescence, and area under the curve (AUC) values are shown. Mean pixel intensities of the two micrographs: 45 (− Atto 610) and 2239 (+ Atto 610). Scale bar: 200 μm. (d) Lanthanide lumiphore excitation saturates at less than 2% in the presence of an LRET acceptor, demonstrating the limitations of LED illumination. Eu^{3+}/ATBTA-functionalized beads were imaged by time-resolved microscopy with varying illumination pulse widths. Representative micrographs of beads imaged in the absence or presence of 10 μM Atto 610 are shown. Scale bar: 200 μm. (e) Average pixel intensities for representative individual beads in (d). The data were fit to the equation in Supplementary Fig. 5 to determine an LED-induced excitation rate (k_{ex}) of 357 ± 56 s^{-1} (s.e.m., n = 5 beads). (f) Predicted excitation curves in the absence or presence of an LRET acceptor.

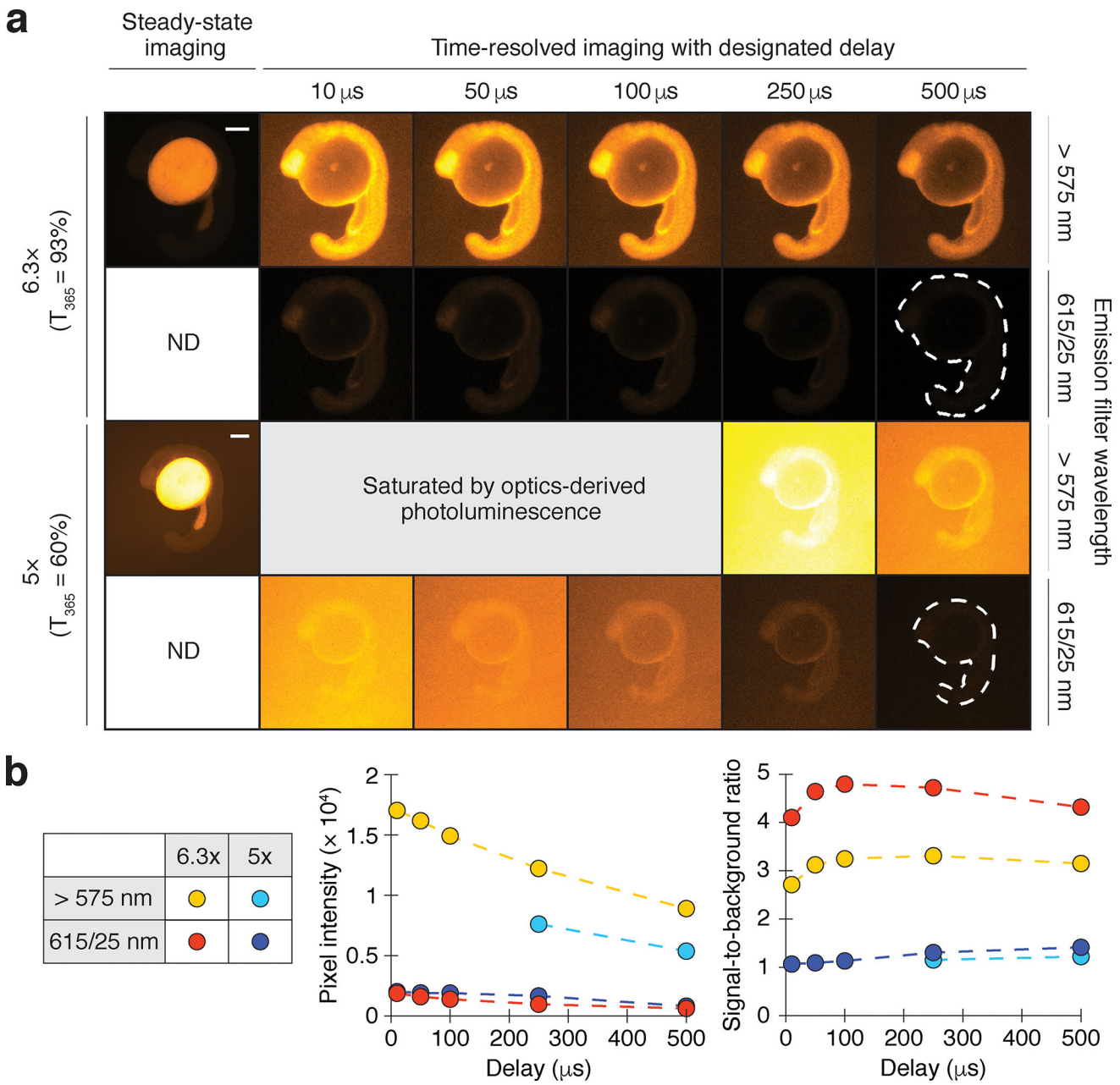

Figure 3. Optics and lanthanide photoluminescence overlap temporally and spectrally

(a) Zebrafish embryos injected with Eu^{3+}/DTBTA-dextran (30 fmol/embryo) and then imaged by objectives with differing UV transmission efficiencies. Emission filters and time delays were also varied to assess the spectral and temporal properties of the optics-derived luminescence. Representative micrographs of 16-hpf embryos are shown. Scale bar: 200 μm. (b) Left graph: average pixel intensities within the embryos (dashed outlines). Right graph: signal-to-background ratios of the time-resolved micrographs, with background defined as average pixel intensities outside the dashed outlines. ND, not determined.

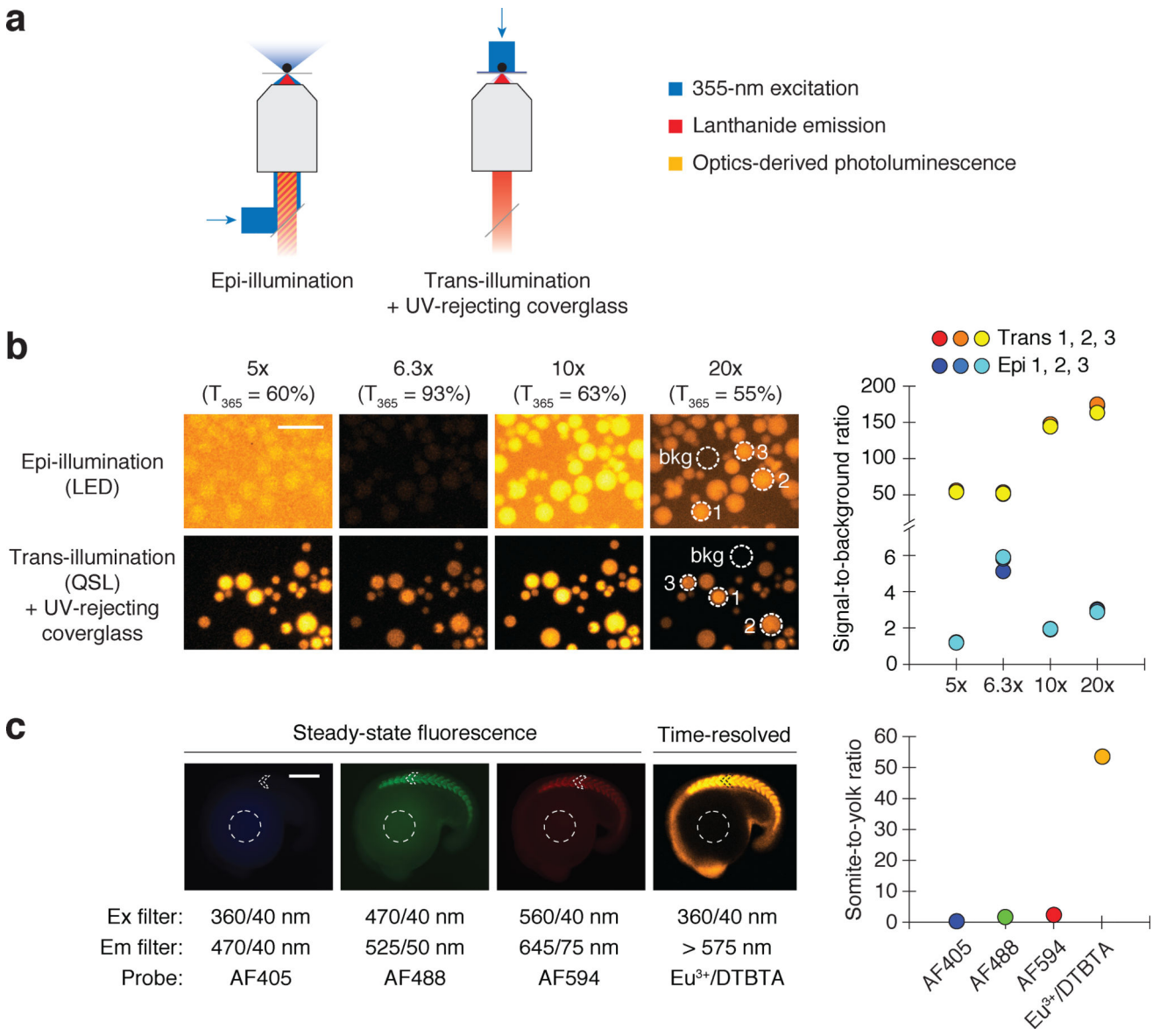

Figure 4. QSL trans-reflected illumination overcomes optics-derived photoluminescence

(a) Optical paths of conventional epi-illumination (left) and trans-illumination (right) microscopy. The trans-illumination configuration also includes a UV-rejecting, TiO_2-coated coverglass placed between the sample and the objective. (b) Eu^{3+}/ATBTA-functionalized beads imaged by time-resolved microscopy, using the designated objectives and either LED epi-illumination or QSL trans-reflected illumination. Signal-to-background ratios for selected beads (dotted circles) are shown. Scale bar: 200 μm. (c) Zebrafish embryos immunostained with an anti-MYH1E primary antibody and a secondary antibody conjugated with the designated probe. Steady-state fluorescence and time-resolved lanthanide luminescence micrographs of 16-hpf embryos and their corresponding somite-to-yolk pixel intensity ratios are shown. Scale bar: 200 μm.

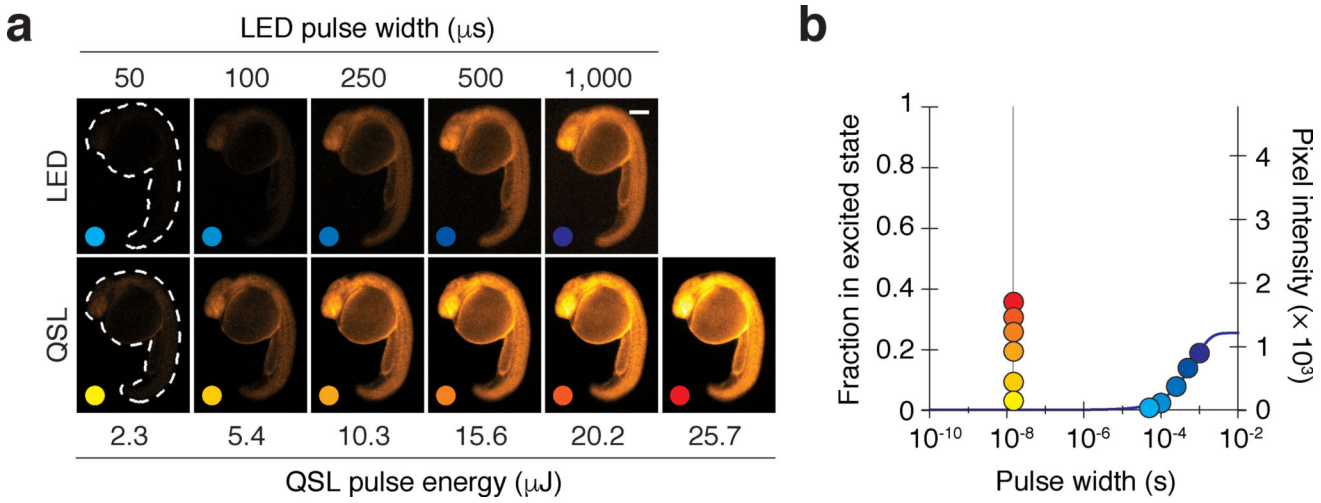

Figure 5. QSL excitation dramatically increases lanthanide excitation rates

(a) Zebrafish embryos injected with Eu^{3+}/DTBTA-dextran (60 fmol/embryo) and then imaged by time-resolved microscopy with a high-UV transmittance objective and varying LED pulse widths or QSL pulse energies. Representative micrographs of 22-hpf embryos are shown. Scale bar: 200 μm. (b) Excited-state fractions and signal intensities of the lanthanide lumiphore for each illumination condition. The predicted excitation level is shown as a solid blue line (R^2 = 0.985). QSL illumination can achieve 20% excitation within 15 nanoseconds (vertical gray line), whereas LED illumination requires a millisecond.

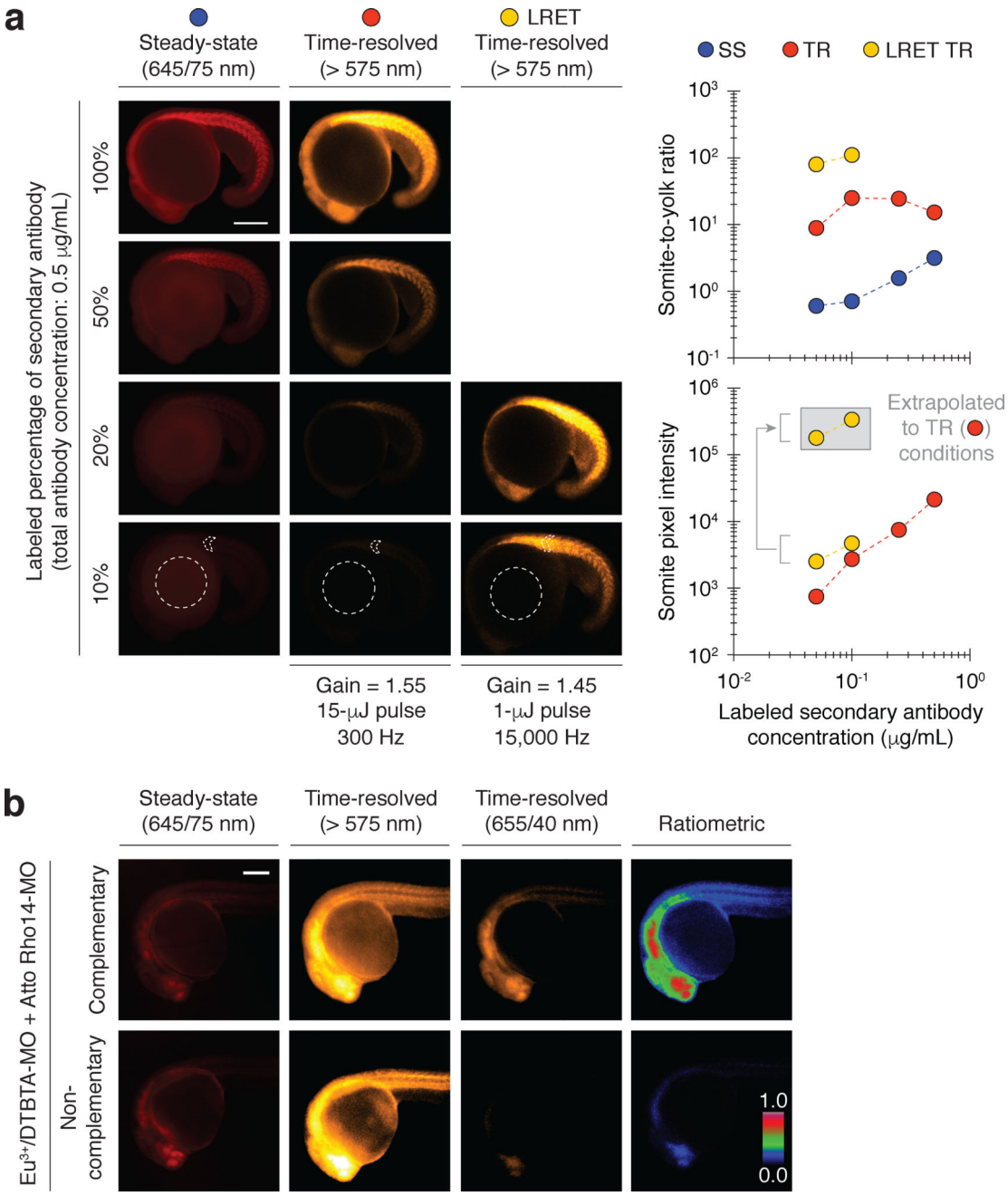

Figure 6. trLRET enables ultrasensitive lanthanide imaging *in vivo*

(a) Zebrafish embryos immunostained with a fixed concentration of anti-MYH1E primary antibody (15.3 μg/mL) and varying concentrations of AF594- or Eu^{3+}/DTBTA-conjugated secondary antibody. The Eu^{3+}/DTBTA-labeled embryos were imaged without or with LRET (30 μM Atto 610), using the designated camera gain, QSL pulse energy, cycle frequency, and emission filter. Representative micrographs of 18-hpf embryos and their corresponding somite-to-yolk pixel intensity ratios and somite pixel intensities are shown. LRET pixel intensities normalized to the camera gain and QSL pulse energy used for non-LRET imaging are shown in the gray box. (b) Steady-state fluorescence and time-resolved luminescence

micrographs of zebrafish embryos (24 hpf) injected at one-cell stage with a Eu^{3+}/DTBTA-labeled morpholino oligonucleotide (MO) and either a complementary or non-complementary MO labeled with Atto Rho14 (20 fmol of each MO per embryo; final *in vivo* concentrations of ~ 400 nM each). The emission filter used for each imaging modality is shown, and ratiometric micrographs were generated by normalizing LRET (time-resolved, 655/40-nm) pixel intensities to those of steady-state Atto Rho14 fluorescence. The maximum ratiometric value was set to unity, resulting in mean values of 0.079 (complementary MOs) and 0.006 (non-complementary MOs) for the micrographs. Scale bars: 200 μm.